ADVANCED ELECTRONIC MATERIALS Open Access
www.advelectronicmat.de

High Gain Derived from Facile Carrier Dynamics Manipulation for Sensitive X-ray Detection and Imaging

Shilin Liu, Yijing Ding, Xin Wang, Yuwei Li, Jing Chen, Zhiwei Zhao, Zhuoya Zhu, Jun Wu, Omolola Esther Fayemi, Byung Seong Bae, Ying Zhu, Wei Lei, Xiaobao Xu,* and Qing Li**

Signal amplification is vitally important for sensing low-dose X-rays in medical diagnosis by amplifying the generated electric read-out signal. However, the complexity of external amplification circuits hampers device miniaturization and portability, while integrating amplification functionality directly into sensors or detectors remains a significant and formidable challenge. In this work, a direct high-gain X-ray detector with facile electron drift speed manipulation is reported in perovskite single-crystal film (SCF). By employing laser-assisted nucleation, high-quality $MAPbBr_3$ SCF is fabricated with precise control of thickness from ≈20 to ≈500 µm and the area up to 3 by 2 cm, while the architecture of ITO/$MAPbBr_3$/Au is constructed to form the Schottky junction in opposite polarity. With the assistance of applied bias, the space electric field over $MAPbBr_3$ SCF can be tunable, which ensures the manipulation of charge carrier drift speed to form recirculation for internal gain. The resultant photodetector exhibits an ultrahigh sensitivity of 1.44×10^5 µC Gy^{-1} cm^{-2} with a gain of 5.14×10^5, an ultralow detection limit of 39.8 nGy s^{-1}, and the X-ray array imaging is achieved at a low dose rate of 5 µGy s^{-1}. These results confirm the advance of high-gain detectors in constructing sensing arrays for practical safe medical diagnosis.

1. Introduction

Signal amplification is an imperative and common in electronic and optoelectronic devices for extracting the weak valuable information.[1] Take X-ray imaging as an example, although sensitive X-ray imaging plays an important role in medical diagnosis, it is well known that the ionizing radiation of X-ray will bring the damage to biologic cells, which is absolutely harmful to human health. So, the detection or imaging of X-ray in the medical diagnosis require the dose as low as possible.[2] However, the precise recognition of tiny difference or change in tissues from X-ray tomography requires a proper dose to obtain high-definition image. As a result, a contradiction forms between a safe dose and high-definition imaging requirement, since the imaging of low-dose X-ray always results in dim outline, which would lose the useful signal. At the current stage, even though the amplification used in X-ray imaging mainly relies on the auxiliary electronic circuit under the assistance of a scintillator for the indirect detection, it still suffers from the limit of array area and complicates fabrication processing.[2b,3] Actually, the forthcoming energy resolution with the photon counting technique in X-ray imaging for identifying the biological tissue details also strictly relies on the efficient signal amplification.[4]

In general, the realization of electric amplification for detection can be divided into two categories: external amplification and internal amplification. The external amplification relies on the signal amplification circuit with reasonable arrangement of electronic elements. Even though the external amplification has been widely accepted and used in the electric data processing of

S. Liu, Y. Ding, X. Wang, Y. Li, J. Chen, Z. Zhao, Z. Zhu, J. Wu, W. Lei, X. Xu, Q. Li
Joint International Research Laboratory of Information Display and Visualization
School of Electronic Science and Engineering
Southeast University
Nanjing, Jiangsu 211189, China
E-mail: lw@seu.edu.cn; xiaobaoxu@seu.edu.cn; liqing@seu.edu.cn

O. E. Fayemi
Department of Chemistry
School of Mathematics and Physical Sciences Faculty of Natural and Agricultural Sciences North-West University
Mafikeng Campus, Private Bag X2046, Mmabatho 2735, South Africa

B. S. Bae
Department of Electronics &Display Engineering Hoseo University
Hoseo Ro 79, Asan city, Chungnam 31499, Republic of Korea

Y. Zhu
E-xray Electronic Co. Ltd.
Suzhou 215131, China

The ORCID identification number(s) for the author(s) of this article can be found under https://doi.org/10.1002/aelm.202300555

DOI: 10.1002/aelm.202300555

X-ray imaging, it would inevitably introduce the additional electric noise and subsequently limit the signal noise ratio.[2b,5] Thus, it has motivated the extensive exploration of internal amplification to avoid the unwanted noise from external circuit. At current stage, the avalanche effect originating from chain collision ionization in depleted junction under high electric field has been the common approach for realizing the internal electric amplification in sensing weak signal.[6] Although the technique of constructing avalanche detectors is becoming mature including the Si-type detector for visible light and InGaAs-type detector for infrared photons, the light atom of Si and InGaAs make them not suitable for directly sensing X-ray. Even worse, the complicate procedure in fabricating avalanche detectors array also hampers their universal application in indirect detecting of X-ray with the assistance of scintillator.

Alternatively, the phenomenon of carrier recirculation has attracted much attention for constructing the novel photoelectric multiplier. Up to now, the exploitation of such functionality undergo the admirable progress in organic photodetector, 2D material-based photodetector, etc. As well, most of the reported gain has exceeded 10^2, which confirms the potential of carrier recirculation for realizing internal amplification above noise floor in the modern read-out electronics.[7] Notably, although the reported high-gain detectors bring the new possibility and lay a solid theoretical foundation for developing detector with internal amplification, the active material of organic material or 2D material can not afford the efficient stopping power for sensing X-ray. Thus, the pursuit of internal amplification for direct low-dose X-ray detection is still a challenge due to the lack of proper sensing materials.

In the past few years lead halide perovskites have attracted intensive academic attention due to their unique optoelectronic properties for application in high-performance solar cells,[8] light-emitting diodes,[9] solid-state lasers[10] and high-sensitivity photodetectors.[11] The high average Z value together with the noble characters of long carrier lifetime, long carrier diffusion length and high defect tolerance render perovskite as candidate in X-ray sensing and imaging.[7d,12] Since Yakunin and his coauthor demonstrated the lead halide perovskites as active material in X-ray sensing, it have proven the success in both direct X-ray and indirect X-ray sensing and imaging.[13] Intriguingly, the performance of reported X-ray detectors with perovskite is comparable or even suppressed that in commercial detector with α-Se or CsI(Tl).[14] More importantly, the high elemental abundance and solution-process preparation also make perovskite one of the most promising materials for universal application in commercial X-ray sensing and imaging.

In this work, a high-gain X-ray detector using $MAPbBr_3$ single crystal film (SCF) as active material is demonstrated with facile Schottky junction engineering. Since the properties of sensing materials play a decisive role in the device performance, the laser-assisted nucleation and growth is employed to control and adjust the preparation of high-quality $MAPbBr_3$ SCF with tunable thickness from ≈20 μm to ≈500 μm and the area up to 3 cm by 2 cm. The obtained $MAPbBr_3$ SCF possesses a low trap density of $\approx 10^{11,}$ that efficiently suppresses the charge recombination (leakage current) and ensures the moderate mobility-lifetime product for efficiently collecting generated charge carriers. As a consequence, the $MAPbBr_3$ SCF with thickness of 29.7 μm is selected to construct the device with the architecture of ITO/$MAPbBr_3$/Au to realize the high gain. Systematic characterizations reveal that the direction of applied bias show a significant influence on the space electric field, in which the positive bias on ITO (Au connecting to ground) enhance the formation of space electric field along the same direction over the whole device and subsequently facilitate the speed of electron drifting to external circuit. The fast drift and short transit time leads to the recirculation of electron before recombination for gains. Thus, a high gain is achieved in our detector with value of $\approx 10^5$ for X-ray photons with a low sensing limit of 39.8 nGy s^{-1}. The successful proof-of-concept low-dose X-ray imaging accompanied with our sensing array will push it forward to practical application.

2. Results and Discussion

To developing the sensitive X-ray detector, the $MAPbBr_3$ possessing the moderate atoms and optoelectronic properties is selected as active materials. **Figure 1**a depicts the schematic diagram of the $MAPbBr_3$ single crystal film (SCF) preparing process. The details of $MAPbBr_3$ SCF fabrication can be found in Experiment Section. In brief, to improve the SCF quality and accurately control their morphology, the laser irradiation is used to control the nucleation. Figure S1 (Supporting Information) shows the temperature distribution around laser spot during the crystal nucleus forming. Due to the character of nucleation at high temperatures, the crystal nucleus first formed at the focus of laser in the solution. It means the laser irradiation allows the manipulation of the number of crystal nuclei, which is beneficial for the following $MAPbBr_3$ SCF growth with large area. Figure 1b presents the photograph of the difference in nucleation with/without laser irradiation. Under laser irradiation, only one crystal nucleus is observed in the solution, while the number of crystal nucleus is uncontrollable by using temperature to promote the nucleation. Once a stable nucleus form under laser irradiation, the confined space is used at 80 °C to grow high-quality and large-size crystal film. Figure S2 (Supporting Information) shows the process of laser-assisted seed crystal growth into a large area single crystal film. Under the assistance of space-confined method, the thickness of as-fabricated $MAPbBr_3$ SCF can be tunable from ≈20 to 500 μm (Figure 1c), in which the solute ions accelerate the nucleus growth along out-of-plane direction. As a result, the area of SCF up to 3 cm by 2 cm can be realized (Figure 1d). To our best knowledge, this is the largest SCF from one nucleus with solution processing (Table. S1, Supporting Information), which verifies the advantage of using laser to facilitate the $MAPbBr_3$ SCF fabrication.

Figure 2a presents the top-view scanning electron microscope (SEM) of as-fabricated $MAPbBr_3$ SCF. The compact and smooth surfaces confirm the continuity in the $MAPbBr_3$ SCF growth, whereas the homogenous element distribution of C, N, Pb, and Br further verify the uniformity in $MAPbBr_3$ (Figure S3, Supporting Information). To provide a visual cognition on the surface, atomic force microscopy (AFM) was conducted. As shown in Figure 2b,c, although there are some tiny $MAPbBr_3$ island on the surface, the root-mean-square (RMS) surface roughness of $MAPbBr_3$ SCF was measured to be 4.2 nm over a scanning area of 5 × 5 μm^2. This result identifies the advance of our solution-processing method for preparing the high-quality

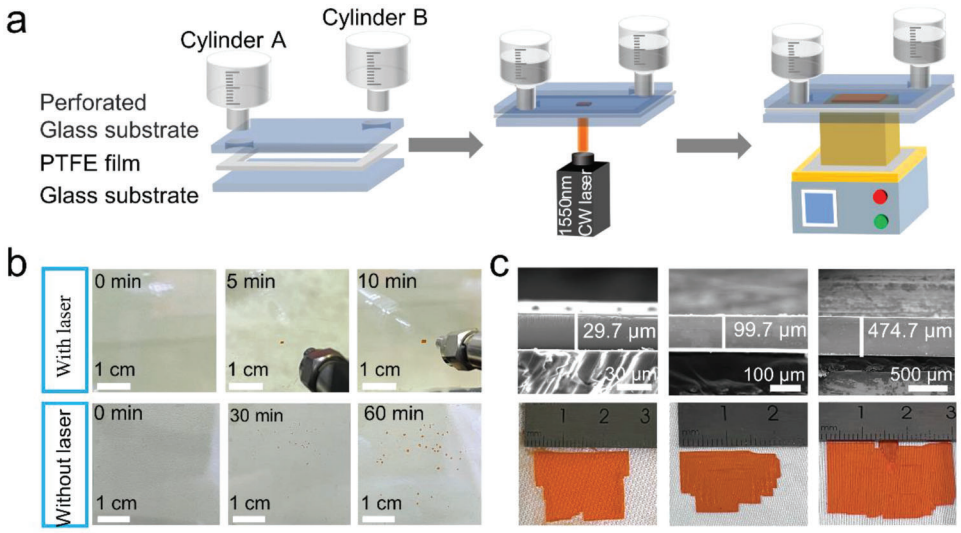

Figure 1. The laser-assisted space-confined method for growing the SCFs with variable thicknesses. a) Sketch map of the laser-assisted space-confined method for growing the SCFs. b) Growth process of the seed crystal with/without laser heating. c) A series of $MAPbBr_3$ SCFs with variable thicknesses of 29.7, 99.7, and 474.7 um. d) Corresponding photos of the $MAPbBr_3$ SCFs with variable thicknesses.

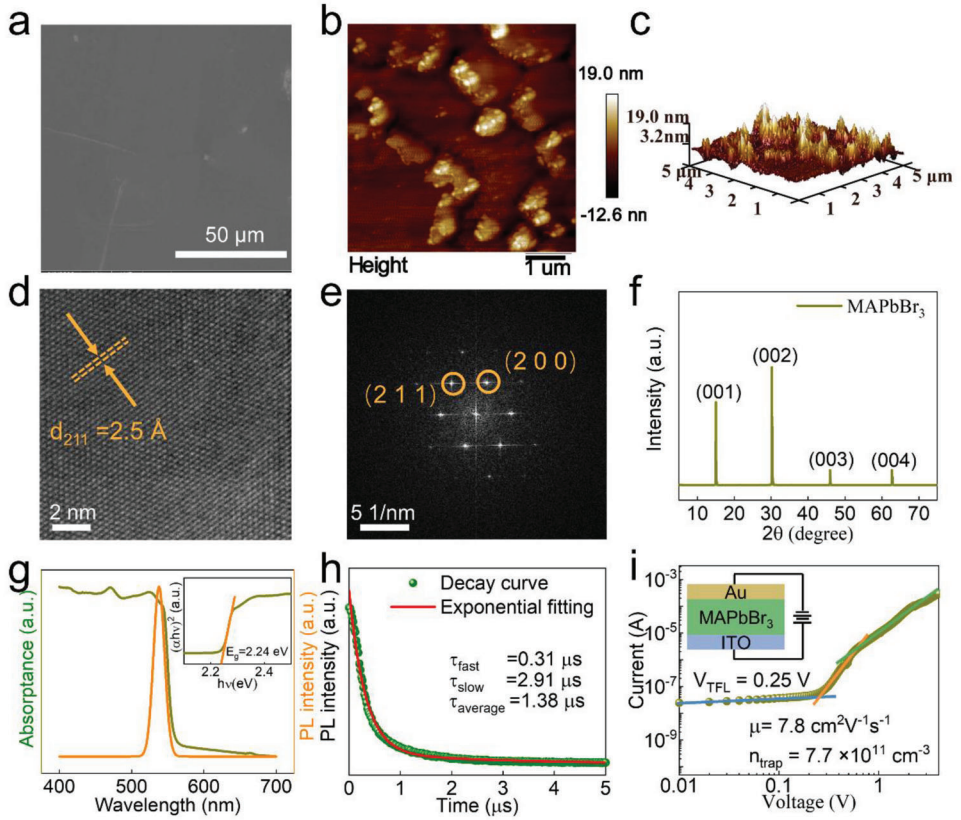

Figure 2. Material and electronic characterization of $MAPbBr_3$ SCF. a) The SEM image of the $MAPbBr_3$ SCF with thicknesses of 29.7 μm. 2 D b) and 3D c) AFM topologies, and the roughness of the surface of $MAPbBr_3$ SCF. d) High-resolution TEM image and e) the corresponding SAED pattern. f) XRD pattern of the $MAPbBr_3$ SCF. g) Normalized PL and absorption spectra of $MAPbBr_3$ SCF. h) The TRPL spectra of $MAPbBr_3$ SCF. i) SCLC characteristics for $MAPbBr_3$ SCF with a thickness of 29.7 μm.

$MAPbBr_3$ film. Figure 2d displays the high-resolution TEM (HRTEM) image of the $MAPbBr_3$ film. The result shows a clear lattice with a spacing of 0.25 nm, which corresponds to the (2 1 1) lattice plane of cubic $MAPbBr_3$ phase. As well, the electron diffraction pattern (Figure 2e) further confirms the single crystal property of the $MAPbBr_3$. Figure 2f shows the X-ray diffraction (XRD) pattern of the $MAPbBr_3$ SCF, which reveals that the as-fabricated $MAPbBr_3$ SCF belongs to the cubic system ($Pm\bar{3}m$) and exhibits an outstanding crystallinity. Together with the smooth surface, the high crystallinity is believed to be beneficial for the device performance due to the enhancement of carrier transport and suppression of carrier recombination (leakage current).[15]

Figure 2g exhibits the intrinsic UV–vis absorption and PL spectrum of the $MAPbBr_3$ SCF, in which the sharp onset at 543 nm refer to the corresponding bandgap (Eg) of 2.24 eV. As well as the photoluminescence (PL) at 538 nm, it is consistent with the previous reports on $MAPbBr_3$ SC.[16] It is worth to note that the absorption spectra show a red shift as thickness increases (Figure S4, Supporting Information) due to the enhancement in band-edge absorption. Since the proposed gain originates from the charge carrier recirculation, the carrier lifetime is a crucial factor in determining gain value according the equation $G = \tau_{lifetime} / \tau_{tr}$. To clarify the potential of $MAPbBr_3$ SC for high gain, the carrier dynamics was investigated with time-resolved PL under an excitation light of 365 nm. As observed, the transient PL presents a character of two-exponential decay (Figure 2h), in which the lifetime is estimated to be 1.38 µs. The long carrier lifetime sets the precondition for carrier recirculation to realize high gain. To further get the insight into the reason of long carrier lifetime, the space-charge limited current (SCLC) measurement was conducted. As illustrated in Figure 2i, the *I*–*V* curve can be divided into three regions, a linear Ohmic region (blue), the trap-filled region (orange), and the trap-free Child's region (green). The trap density (n_{trap}) can be clearly deduced according to trap-filled limit voltage (V_{TFL}) by using the following equation[11b]:

$$V_{TFL} = \frac{e n_{trap} L^2}{2\varepsilon\varepsilon_0} \tag{1}$$

where V_{TFL} is the TFL voltage, e is the elementary charge, n_{trap} is the defect density, L is the film thickness, ε_0 is the vacuum permittivity and ε is the relative dielectric constant of $MAPbBr_3$ (25.5).[17] The calculated n_{trap} of $MAPbBr_3$ SCF is 7.7×10^{11} cm^{-3}, which is comparable to reported bulk single crystal and several orders of magnitude lower than polycrystalline films.[16a,18] It is worth noting that as the thickness of the single crystal film increases from 29.7 to 474.7 µm, there is a decrease in defect density from 7.7×10^{11} to 1.9×10^{11} due to the reduction in specific surface area (Figure 2i; Figure S5, Supporting Information). Meanwhile, the carrier mobility (μ) was also calculated by fitting the Child region (red) with Mott–Gurney's equation[19]:

$$J_D = \frac{9\varepsilon_0\varepsilon_r \mu V^2}{8L^2} \tag{2}$$

in which J_D is the current density and V is the applied voltage. The μ of $MAPbBr_3$ SCF is estimated as 7.8 cm^2 s^{-1} V^{-1}, which ensures the fast carrier transit over the lifetime.

Considering the balance between stopping power for X-ray and carrier collection, the thickness of 29.7 µm in $MAPbBr_3$ SCF was selected to develop the high-gain X-ray detector. To foster this high-gain detector, two different architectures were constructed including an asymmetric electrode structure of ITO-$MAPbBr_3$-Au and a symmetric electrode structure of Au/$MAPbBr_3$/Au. **Figure 3**a,b depicts the schematic diagram of device architecture and the corresponding energy level of each layer. The energy level of $MAPbBr_3$ SCF was extracted from UV photoelectron spectroscopy (Figure S6, Supporting Information) with valence band maximum at −5.56 eV, fermi level at −4.52 eV and conduction band minimum at −3.32 eV. Kelvin probe measurements (Figure S7, Supporting Information) indicate the energy differences between $MAPbBr_3$ SCF and electrodes are ≈0.47 and ≈0.17 V for Au and ITO, respectively, which further convinces the energy diagram in $MAPbBr_3$ SCF. Figure 3c presents their *I*–*V* curves under irradiation and in dark. The asymmetric device displays a rectifying behavior. More importantly, the remarkable difference between the dark current and photocurrent at zero bias demonstrates the excellent self-powered behavior of the ITO-$MAPbBr_3$-Au device. Figure S8 (Supporting Information) shows the *I*–*V* curves of the ITO-$MAPbBr_3$-Au and Au-$MAPbBr_3$-Au devices under 525 nm LED illumination, respectively, with light power density ranging from 38.22 nW cm^{-2} to 10.19 mW cm^{-2}. The photocurrent increases rapidly at the lower voltage, and then the increasing rate decreases due to the saturation effect of the photocurrent as the voltage further increase. The resulting gain can be calculated by $G = \frac{(J_{light} - J_{dark})/e}{P/h\nu}$, where e is electronic charge and $h\nu$ is the incident photon energy. Figure 3d shows the extracted gain of two devices under different biases depending on the illumination power of 525 nm light. In the asymmetric detector, the gain increases as the incident light power decreases under 2 V bias (Au connected to ground). Due to limit of experiment condition, our detector reaches a gain maximum of 3.12×10^5 at 38.22 nW cm^{-2}. In comparison, the symmetric device shows almost no gain. This result implies the device architecture plays a vital role in pursuit of internal gain with carrier recirculation. Notably, when the bias is 0 and −2 V, the device shows a negligible gain.

To better evaluate the asymmetric detector, other figure-of-merit parameters are also measured. Figure 3e shows its dark current density being 1.35 nA cm^{-2} under an bias voltage of 0 V, which is much smaller than that under the bias voltage of −2 and 2 V, respectively. To further clarify the resolution in sensing weak signals, we next investigated the noise current by using fourier transform (FFT) of time-dominated dark current at different voltages. As shown in Figure 3f, frequency-independent noise currents of the devices under the bias voltages of 0, −2, and 2 V are 2.45×10^{-13}, 6.82×10^{-12} ,and 2.42×10^{-8} $Hz^{-1/2}$ at 1 Hz, respectively. It should be noted that the frequency-independent noise currents undergo the same change tendency along the applied bias voltages, which matches well with the variation of dark current (Figure 3e). This result indicates the internal gain amplifies the noise as well as the generated electric signal. This is reasonable due to the failure of distinguish the electric signal originating leakage current or not. Moreover, the response rate in our asymmetric detector are also checked. Figure 3g shows the response to temporal light. The rise and decay times of

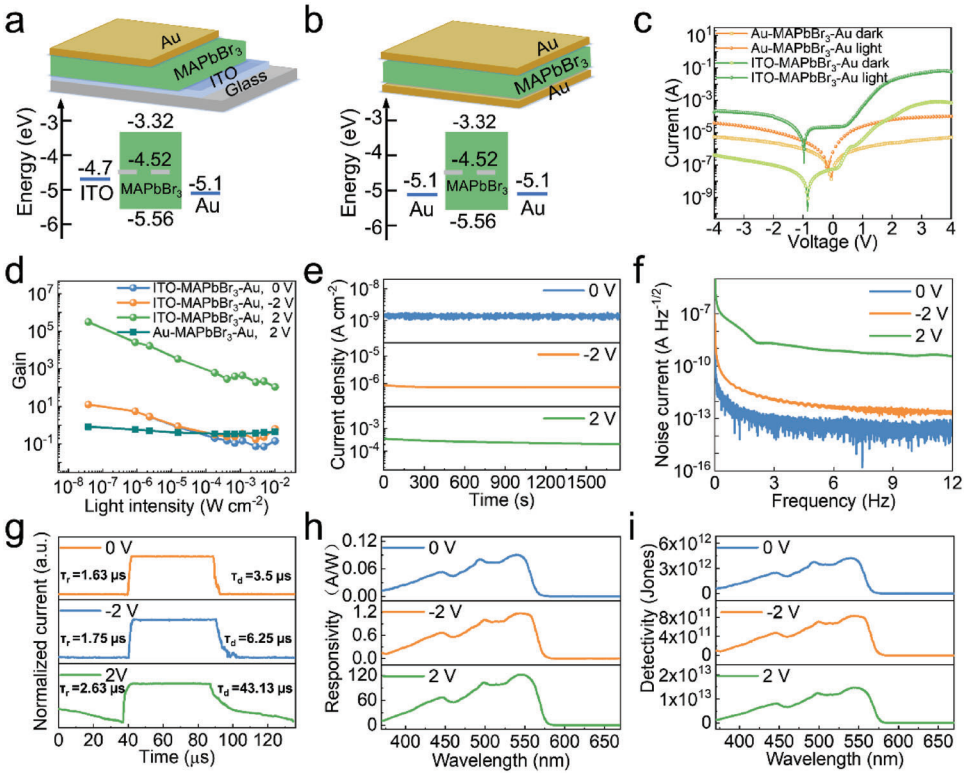

Figure 3. The electrode structure and biases effect on the performance of $MAPbBr_3$ SCFs detector. Schematic image and energy-level diagram of a) a asymmetric electrode structure of ITO-$MAPbBr_3$-Au and b) a symmetric electrode structure of Au/$MAPbBr_3$/Au. c) Logarithmic I–V curves of $MAPbBr_3$ SCF based devices with different electrode structures. d) Light-intensity-dependent gain of two photodetectors measured at various biases. e) Dark current drifts of SCF photodetector under various biases. f) Measured dark-current noise of the photodetector at various biases. g) Light response of rise and decay time of the SCF photodetector. h) and i) are responsivity and detectivity of the SCF photodetector with different bias voltages under incident light at wavelengths of 300–650 nm.

response are estimated to be 1.63 and 3.5 μs, 1.75 and 6.25 μs, 2.63, and 43.13 μs for the bias of 0, −2 and 2 V, respectively. The continuous temporal response of device to on/off switching signal under different bias can be found in Figure S9 (Supporting Information). The fast switching behavior endows the promise of high-speed detection, together with signal amplification, it is of importance for realizing dynamic imaging with high frame rate toward low-dose X-ray. Figure 3h gives the responsivity (R) toward sensing the visible photons. Benefit from the high gain, the peak responsivity reaches 0.09,1.18 and 121.87 A/W under the bias voltages of 0, −2 and 2 V, with the corresponding D^* being 4.21×10^{12}, 8.29×10^{11}, and 1.73×10^{13} (Figure 3i), respectively. Table S2 (Supporting Information) presents a comparison of the key parameters of various single-crystal thin film devices with different structures and types. The results verify the superior responsivity and detectivity in our device due to the ultrahigh gain.

To give an insight into the mechanism of gain in asymmetric device and clarify the role of Schottky junction, the simulation with finite element method from Comsol software was employed. For the visual comparison, the simulation was conducted with different bias. **Figure 4**a-i,b-i presents the calculated the energy level alignment in asymmetric device under different bias. As observed, there is a turning point in CBM and VBM energy bands of $MAPbBr_3$ SCF under negative bias, which localize at the place with distance of 2 μm to ITO electrode. Notably, this turning point disappears under positive bias. To further identify the origin of turning point, the distribution of electric field was also simulated (Figure 4a-ii,b-ii). As expected, the electric field along the $MAPbBr_3$ SCF is divided into two parts and they are along completely opposite direction under negative bias (Au is ground electrode). Briefly, the electric field shows a sharp change near Au electrode due to the large difference of energy level between Au and Fermi level in $MAPbBr_3$ and the direction changes at the turning point. The details can be found in Figure 4a-i and Figure S10 (Supporting Information). It means the extraction of photogenerated carrier in $MAPbBr_3$ SCF would inevitably undergo speed up and speed down. Instead, although the electric field also show the sharp change around Au electrode, it goes along the same direction over the whole $MAPbBr_3$ SCF under positive bias on ITO (Figure 4b-ii; Figure S10, Supporting Information). The electric field along the same direction ensures the drift speed of photogenerated charge carriers undergo continual increase during the extraction from $MAPbBr_3$, and subsequently facilitate the carrier recirculation.

To confirm the difference of electric field in the devices under positive and negative bias, the cross-section SEM was conducted with the mode of secondary electron, in which the electric field over the material has a significant influence on the escape of secondary electron. As we can see from Figure 4c, the grayscale

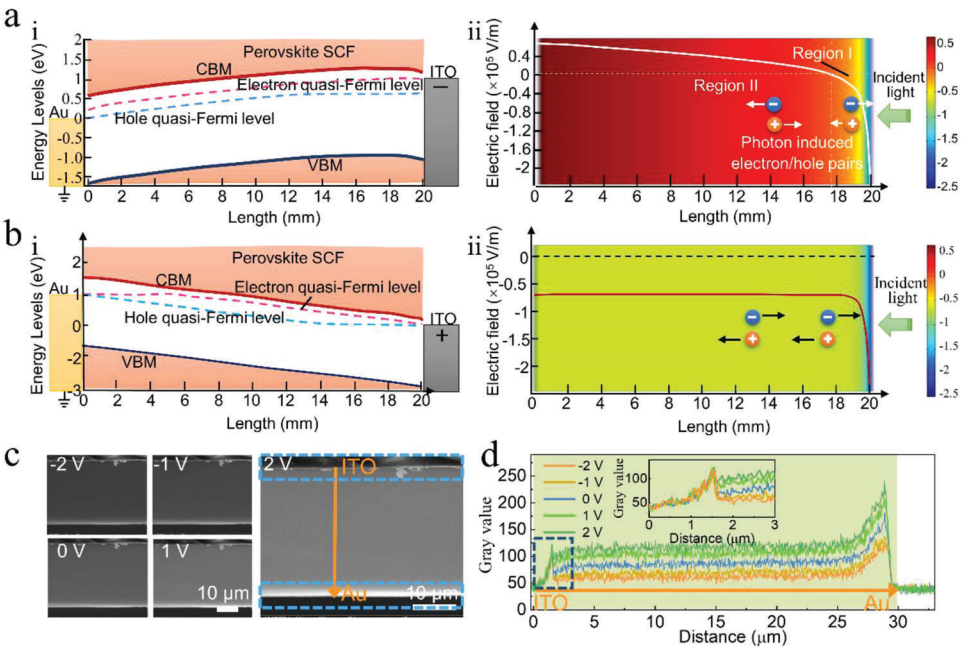

Figure 4. Band structure of detector and dynamic transport process of carriers. a) Band structure of detector i) and photogenerated carrier transport ii) in the detector, when Au electrode is grounded and ITO is applied with a −1 V bias. b) Band structure of detector i) and photogenerated carrier transport ii) in the detector, when Au electrode is grounded and ITO is applied with a +1 V bias (a and b are the results of numerical calculations by Comsol software). c) SEM images of the SCF photodetector under different voltage bias (The gray value of SEM image at ITO/$MAPbBr_3$ and Au/$MAPbBr_3$ interfaces exhibit voltage-dependent variations, suggesting that the space charge region changes with voltage) and d) line profile of SEM image gray value as a function of width.

in device under negative bias shows an obvious change around Au electrode (≈2 μm), which coincides with the simulation results. Figure 4d provides the change of grayscale over the whole $MAPbBr_3$ SCF under different bias. In general, the negative electric field can promote the secondary electron escape, while the positive field hinders the secondary electron escape. As expected, the cross-section of device presents a light gray under positive bias in comparison with that under negative bias. As well, all the devices show the difference in grayscale around Au electrode. It indicates the negative electric field cover the whole $MAPbBr_3$ under the work condition of positive bias (ITO), which is same as that in simulation (Figure 4b-ii). This is believed to be the reason for the realization of high gain in the asymmetric device. To verify this perspective, we can calculate the transit time for carriers to drift in the detector based on the electric field distribution of the detector according to the following equation:

$$t_{drift} = \int_0^{length} 1/\left(E\left(x\right) \cdot \mu \cdot V\right)\, dx \tag{3}$$

The transit time of electrons is ≈0.16 ns when the bias voltage of the ITO electrode is 2 V (Figure S11, Supporting Information). The gain was estimated to be 10^4, which gives the qualitative explanation for the signal amplification in our detector.

Since we have confirmed the gain and established its work mechanism in our detector, we further evaluate its sensing performance toward low-dose X-ray. Figure S12a (Supporting Information) displays the attenuation coefficient of $MAPbBr_3$ to X-ray. As the α-Se is used in the commercial direct X-ray sensing and imaging for medical diagnosis, it is selected for comparison. It is obvious that $MAPbBr_3$ possess a better stopping power and even 29.7 μm $MAPbBr_3$ can have a harvesting efficiency of 11.04% for 40-keV X-ray photon (Figure S12b, Supporting Information). **Figure 5**a displays the on/off responses of the detector under X-ray illumination with different dose rates. The signal under 2 V is almost 4 and 3 order magnitude larger than that under 0 V and −2 V, respectively. The exact value of photocurrent is presented in Figure 5b, in which the generated current density shows a linear relationship with the X-ray dose rates. The sensitivity of the X-ray detector can be estimated by fitting the slope of the photocurrent density-dose rate curves, whereas the sensitivity of the device under 0, −2, and 2 V was calculated to be 71, 2163 and 1.44×10^5 μC Gy_{air}^{-1} cm^{-2}, respectively. The gain factors (G) of this device under 90 μGy_{air} s^{-1} X-ray were estimated according to $G = \frac{I_R}{Ip}$, in which I_p is the theoretical response current induced by impact ionization and I_R is the response current. The theoretical current (I_p) has been calculated according to the equation[20]:

$$I_p = \beta\varphi\eta e \tag{4}$$

in which β is the flux of X-ray photons, φ is the X-ray absorption efficiency of the device, and η is the number of electron-hole pairs generated by a high-energy X-ray photon. Considering the SCF thickness of 29.7 μm in our research, it has a 11.04% absorption efficiency (ϕ is 11.04%). The electron-hole pair generation energy W can be estimated by the empirical equation $W = 2Eg + 1.43\ eV$.[7c,20b] The number of electron-hole pairs generated by a high-energy X-ray photon is expressed as $\eta = E_{ph}/W$,

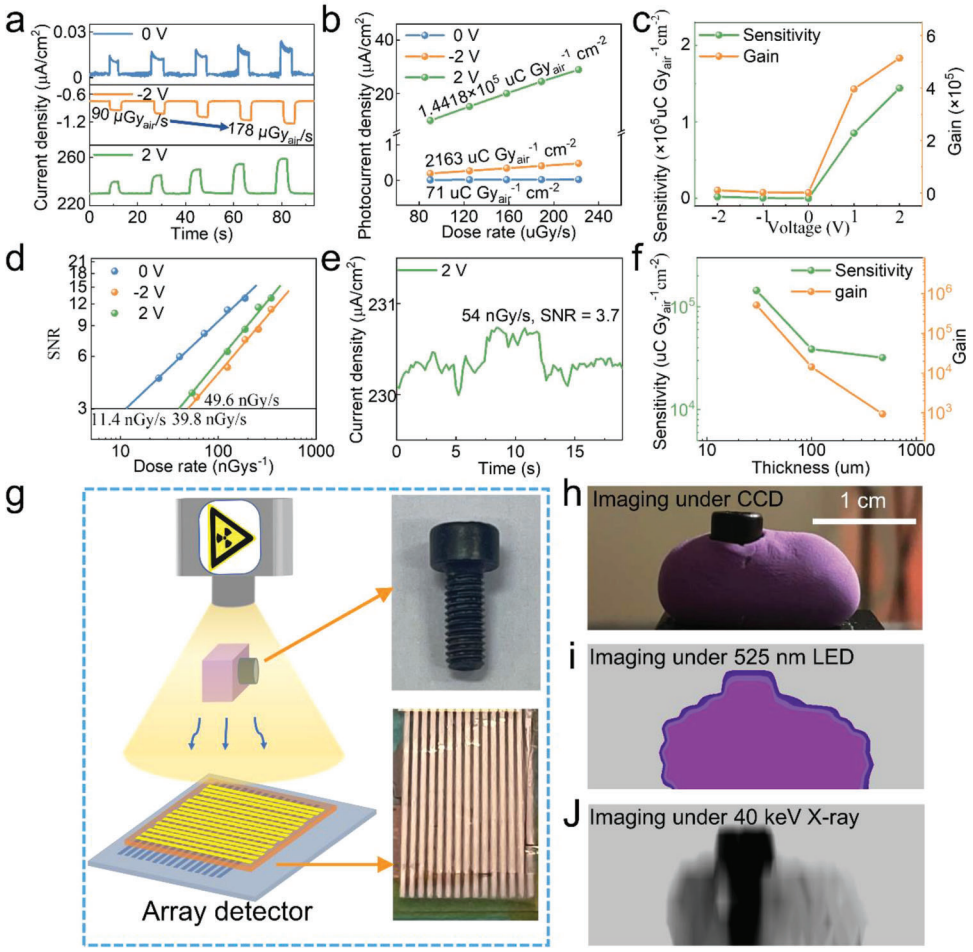

Figure 5. X-ray detection performance and array imaging. a) X-ray response current curve of the device under various biases. b) X-ray response current of the device at different dose rates under biases of 0 V, −2 V, and 2 V. c) The sensitivity and gain factors of the device under 90 $\mu Gy_{air}\ s^{-1}$ X-ray illumination. d) Dose rate-dependent SNR of the X-ray response for the detector. e) The X-ray response of the detector under biases of 2 V at ultralow doses. f) The thickness-dependent sensitivity and gain factors of $MAPbBr_3$ SCF device under biases of 2 V. h) Schematic of the X-ray imaging process based on the SCF detector array. i) Optical image of a screw wrapped in plasticine. Corresponding visible image j) and X-ray image k) at a dose rate of 5 $\mu Gy_{air}\ s^{-1}$ under bias of 2 V.

where E_{ph} is the average energy of X-ray photons being 40 keV in this research. The flux of X-ray photons through the detector can be expressed as $\beta = Dm_s/Eph$, In which D is the dose rate of X-ray, m_s is material weight and E_{ph} is the X-ray photon energy. Combining all these factors, the theoretical response current can be expressed as $I_p = Dm_s e/W$ and was estimated to be 5.80×10^{-4} nA. As a result, the gain factor of the device at 0, −2, and 2 V was estimated to be, 6.75×10^2, 1.00×10^4, and 5.14×10^5, respectively (Figure 5c).

The detection limit of X-ray detectors is commonly determined by their sensitivity and noise characteristics, which can vary depending on the voltage applied to the detector. At the voltage of 0 V, the low noise level enables the detection limit to be as low as 11.4 nGy/s, whereas at 2 V, a detection limit of 39.8 nGy/s was realized, which is two orders of magnitude lower than the commercial α-Se (5.5 $\mu Gy\ s^{-1}$)[21] and identify its potential of sensing low-dose X-ray (Figure 5d) signal. Furthermore, Figure 5e shows the X-ray response of the perovskite detector with an ultralow dose rate of 54 $nGy\ s^{-1}$, where an SNR of 3.7 is derived, validating its strong capacity for low-dose X-ray detection. In addition to the detection limit, stability is another concern for devices exposed to high-energy radiation. Perovskite X-ray detectors are susceptible to damage or decay after exposure to large doses of X-rays. Figure S13 (Supporting Information) presents the results of a stability test of the $MAPbBr_3$ SCF photodetector at 2 V. When the photodetector was exposed to X-rays at 90 $\mu Gy_{air}\ s^{-1}$ for 3600 s, the sensitivity decreased only very slightly, from 1.44×10^5 to 1.21×10^5 $\mu C\ Gy^{-1}\ cm^{-2}$. The total dose exposure for the photodetector was 324 mG_{yair}, equivalent to the dose required to obtain >3000 X-ray images of the chest. Overall, our photodetector demonstrates a high sensitivity of 1.44×10^5 $\mu C\ Gy^{-1}\ cm^{-2}$, which is much higher than those of previously reported value (Table S3, Supporting Information). Figure 5f summarizes the influence of thickness in $MAPbBr_3$ SCF on the sensitivity and gain factor. The gain of the $MAPbBr_3$ SCF photodetector decreases rapidly from 5.14×10^5 to 9.30×10^2, and the sensitivity decreases from 1.44×10^5 $\mu C\ Gy^{-1}\ cm^{-2}$ to 3.20×10^4 $\mu C\ Gy^{-1}\ cm^{-2}$ as thickness increases from 29.7 to 474.7 μm. It can be ascribed to the long

transit time before carrier drifted to external circuit in the thick $MAPbBr_3$ SCF.

To further demonstrate the potential of our detector in practical application, the sensing array was constructed and its proof-of-imaging was conducted as shown in Figure 5g. The pixel size was 200 μm× 200 μm and the imaging target is the screw in plasticine (Figure 5h). For the comparison, the imaging of visible photo is also provided. As we can observe, the visible photon imaging can only provide the rough outline (Figure 5i), while the X-ray imaging gives the details of screw (Figure 5j). In addition, we also evaluated the spatial resolution of the X-ray sensing array. The well-acknowledged slanted-edge method was adopted for the modulation transfer function (MTF) measurement.[22] The response to the edge was recorded as the edge spread function (ESF), which was differentiated to obtain the line spread function (LSF), as shown in Figure S14 (Supporting Information). Then, the MTF could be derived by applying a fast Fourier transformation to the LSF. The resulting MTF is presented in Figure S14c (Supporting Information), and the spatial resolution was 4.9 lp mm^{-1} at 20% MTF value, consistent with the pixel size. These results clearly prove that our facile high-gain imaging array can be used in practical cross-section imaging.

3. Conclusion

In summary, a facile high-gain X-ray detector with $MAPbBr_3$ SCF was constructed. To promote the device performance, the laser-assisted nucleation and space-confined growth were employed to fabricate the $MAPbBr_3$ SCF with precise control of thickness from ≈20 μm to ≈500 μm and the area up to 3 cm by 2 cm. Systematic measurements indicate the distribution of electric field in the device has a significant influence on the carrier drift speed, which the applied bias can tune it for adjusting the carrier transit time for recirculation. As a result, a high gain of 3.12×10^5 was realized under 2 V bias, which ensure a champion sensitivity of 1.44×10^5 μC Gy^{-1} cm^{-2} and limit of ≈39.8 nGy s^{-1}. This work will not only prove the potential perovskites-based X-ray sensing devices toward low-dose X-ray, but also pave the way for the exploration of energy resolution in X-ray imaging.

4. Experimental Section

Growth Method of $MAPbBr_3$ SCF: A 1.6 M clear solution dissolving with stoichiometry proportion of MABr (99.5%) and $PbBr_2$ (AR, 99.0%) in N,N-dimethylformamide (DMF) was obtained at room temperature. The glass substrates, PTFE films and Cylinders were ultrasonically cleaned with deionized water, acetone, and alcohol for 30 min, respectively. The growth device of single crystal film consists of two cylinders, a perforated substrate, a spacer layer and a bottom substrate. The perforated substrate, the bottom substrate and the spacer layer were fitted together, and the surrounding was sealed with PDMS. The cylinder A and cylinder B were connected with the holes of the perforated substrate and sealed with epoxy resin glue. Two cylinders were designed along the diagonal of the upper quartz glass sheet for provide raw materials (1.6 M with equal molar amounts of MABr and $PbBr_2$ in DMF). First, the precursor solution was added to the cylinder A and the solution was continuously injected into the confined space that were built by two pieces of glass substrates. Then, the solution was added to the cylinder B. The confined space device was first heated using a 1550 nm CW laser to guarantee that the nucleation occurred at the heating part. The laser power was set as 3 W. After a small $MAPbBr_3$ wafer was observed, the confined space device was put in 80 °C heating plate to grow the single crystal film by inverse temperature crystallization. During the growth of single crystal film, the raw materials in the confined spaces that were built by two pieces of glass substrates to be consumed, and simultaneously the raw materials will be continuously supplied from Cylinder A and Cylinder B by a nature fluid convection due to concentration difference. With self-supply of raw materials from Cylinder A and Cylinder B to the confined spaces, the crystals can be sustained at a stable growth rate. The depth of confined space was controlled by adding PTFE films with different thicknesses in the confined space. The thickness of obtained single crystal film can be controlled in the range of from 10 to 500 μm. The whole period of crystal growth lasted for ≈102 h before the upper perforated substrate was carefully removed. After cooling down, the SCF was wiped dry with filter paper and further cleaned/washed with IPA. Finally, the SCF was collected with tweezers and dried under a flow of N_2.

Detector Device Preparation: A vertical ITO-$MAPbBr_3$ SCF-Au photodetector was prepared. $MAPbBr_3$ SCF was first grown on the ITO substrate. Following that a hard mask had been put on the top surface of the film. A square Au electrode (50 nm in thickness, 2 mm × 2 mm in area) was then thermally deposited on the top surface of the film in the vacuum chamber. For the device for image sensing, $MAPbBr_3$ SCF was first grown on a stripe-shaped array ITO substrate. Then, a 50 nm thick stripe-shaped array of Au metal electrodes was thermally evaporated onto the single crystal film using a shadow mask, oriented perpendicular to the substrate electrode direction.

Characterizations: The XRD patterns were tested using a Rigaku SmartLab SE X-ray diffractometer and Cu Ka radiation (1.5406 Å). The UV–vis absorption spectra were recorded using a spectrophotometer (Lambda 950). The steady-state photoluminescence (PL) spectra were collected with an FS5 spectrofluorometer (Edinburgh Instruments, UK). The time-resolved PL (TRPL) measurements were performed using a picosecond pulsed diode laser for excitation and a time-correlated single-photon counting detector for signal collection. Atomic force microscopy (AFM) and scanning Kelvin probe force microscopy (KPFM) measurements were performed on a Bruker Dimension FastScan AFM system. The surface morphologies and thickness of $MAPbBr_3$ SCFs were characterized by scanning electron microscopy (SEM, Quanta 200 FEI). TEM and HRTEM images were carried out on a FEI Titan 80-300 electron microscope, operating at 180 kV. Ultraviolet Photoelectron Spectroscopy (UPS) was performed by PHI 5000 VersaProbe III with He I source (21.22 eV) under an applied negative bias of 9.0 V. The I–V (current–voltage) and I-T (current-time) curves were recorded by a Keithley 2400 semiconductor analyzer. The responsivity spectra were measured by a joint system of a monochromated 450 W xenon lamp (Oriel) and a source meter (Keithley 2400), and calculated using a calibrated Si photodiode (OS-Optoelectronics). The noise current was extracted from the dark current recorded by an Agilent oscilloscope (7.5G) with a current amplifier. The rise and decay time were obtained by an oscilloscope with a function generator controlling the frequency of the light source (525 nm LED). For the X-ray detection, the device was put on detector panel of X-ray imaging system and Keithley 2400 was used to measure the current and supply the voltage bias in a dark lead room.

Supporting Information

Supporting Information is available from the Wiley Online Library or from the author.

Acknowledgements

This work was financially supported by the National Key Research and Development Program of China (2021YFE0105900 and 2022YFE0139100), the National Natural Science Foundation Project of China (62175028, 51879042, and 61674029), the National Natural Science Foundation Project for Young Researcher (12005038), the Program 111_2.0 in China (BP0719013), the Leading Technology of Jiangsu Basic Research Plan (BK20192003), the International cooperative research project of Jiangsu province (BZ2022008).

Conflict of Interest

The authors declare no conflict of interest.

Author Contributions

S.L. and Y.D. prepared the $MAPbBr_3$ Single crystal film and conducted their material and optoelectronic characterizations. S.L.and X.W. designed and fabricated the device, and collected the data. S.L. analyzed the data and made the figures with the assistance of X.X., J.C., Z.Z., J.W., and O.E.F. W.L., Z.Z., and B.S.B. built the device model and conducted device simulation from Comsol software. S.L., Y.L., and Y.Z. conducted the X-ray imaging characterization. S.L. wrote the first draft, X.X. and W.L. revised the manuscript, and all the authors reviewed the manuscript.

Data Availability Statement

Research data are not shared.

Keywords

high-gain, perovskites, photodetectors, single crystal films, X-ray

Received: August 18, 2023
Revised: September 13, 2023
Published online: October 13, 2023

[1] a) P. Shahbazi-Derakhshi, E. Mahmoudi, M. M. Majidi, H. Sohrabi, M. Amini, M. R. Majidi, A. Niaei, N. Shaykh-Baygloo, A. Mokhtarzadeh, *Biosens.-Basel* **2023**, *13*, 172; b) Y.-H. Lin, W. Huang, P. Pattanasattayavong, J. Lim, R. Li, N. Sakai, J. Panidi, M. J. Hong, C. Ma, N. Wei, N. Wehbe, Z. Fei, M. Heeney, J. G. Labram, T. D. Anthopoulos, H. J. Snaith, *Nat. Commun.* **2019**, *10*, 4475; c) X. Pang, J. Qi, Y. Zhang, Y. Ren, M. Su, B. Jia, Y. Wang, Q. Wei, B. Du, *Biosens. Bioelectron.* **2016**, *85*, 142.

[2] a) L. Liu, W. Li, X. Feng, C. Guo, H. Zhang, H. Wei, B. Yang, *Adv. Sci. (Weinh)* **2022**, *9*, 15; b) H. Wu, Y. Ge, G. Niu, J. Tang, *Matter* **2021**, *4*, 144; c) Y. Liu, X. Zheng, Y. Fang, Y. Zhou, Z. Ni, X. Xiao, S. Chen, J. Huang, *Nat. Commun.* **2021**, *12*, 1686; d) X. Wang, Y. Xu, Y. Pan, Y. Li, J. Xu, J. Chen, J. Wu, Q. Li, X. Zhang, Z. Zhao, C. Li, E. E. Elemike, D. C. Onwudiwe, J. Akram, W. Lei, *Nano Energy* **2021**, *89*, 106311.

[3] a) Y. Wu, J. Feng, Z. Yang, Y. Liu, S. (F.). Liu, *Adv. Sci. (Weinh)* **2022**, *10*, 2205536; b) B. Wang, X. Yang, S. Chen, S. Lu, S. Zhao, Q. Qian, W. Cai, S. Wang, Z. Zang, *iScience* **2022**, *25*, 105593; c) H. Chen, J. Chen, M. Li, M. You, Q. Chen, M. Lin, H. Yang, *Sci China Chem* **2022**, *65*, 2338.

[4] a) F. Liu, M. Yoho, H. Tsai, K. Fernando, J. Tisdale, S. Shrestha, J. K. Baldwin, A. D. Mohite, S. Tretiak, D. T. Vo, W. Nie, *Mater. Today* **2020**, *37*, 27; b) H. Wei, D. Desantis, W. Wei, Y. Deng, D. Guo, T. J. Savenije, L. Cao, J. Huang, *Nat. Mater.* **2017**, *16*, 826; c) Y. He, M. Petryk, Z. Liu, D. G. Chica, I. Hadar, C. Leak, W. Ke, I. Spanopoulos, W. Lin, D. Y. Chung, B. W. Wessels, Z. He, M. G. Kanatzidis, *Nat. Photonics* **2020**, *15*, 36.

[5] a) T. Zou, B. Xiang, Y. Xu, Y. Wang, C. Liu, J. Chen, K. Wang, Q. Dai, S. Zhang, Y.-Y. Noh, H. Zhou, *IEEE J. Electron Devices Soc.* **2021**, *9*, 96; b) L. Xiang, Y. Wang, X. Liu, X. Huang, Z. Xin, Y. Xu, C. Liu, K. Wang, J. Chen, Y. Yang, S. Zhang, H. Zhou, *Flexible Printed Electron.* **2021**, *6*, 015008; c) B. Xin, N. Alaal, S. Mitra, A. Subahi, Y. Pak, D. Almalawi, N. Alwadai, S. Lopatin, I. S. Roqan, *Small* **2020**, *16*, 43.

[6] a) C. Bruschini, H. Homulle, I. M. Antolovic, S. Burri, E. Charbon, *Light Sci Appl* **2019**, *8*, 87; b) J. Zhang, M. A. Itzler, H. Zbinden, J.-W. Pan, *Light Sci Appl* **2015**, *4*, e286; c) J. Michel, J. Liu, L. C. Kimerling, *Nat. Photonics* **2010**, *4*, 527; d) S. Cova, M. Ghioni, A. Lotito, I. Rech, F. Zappa, *J Mod Opt* **2004**, *51*, 1267; e) B. Wang, J. Mu, *Photonix* **2022**, *3*, 8; f) J. Liu, S. Cristoloveanu, J. Wan, *Phys. Status Solidi* **2021**, *218*, 24.

[7] a) W. Pan, B. Yang, G. Niu, K.-H. Xue, X. Du, L. Yin, M. Zhang, H. Wu, X.-S. Miao, J. Tang, *Adv. Mater.* **2019**, *31*, 44; b) M. Hu, S. Jia, Y. Liu, J. Cui, Y. Zhang, H. Su, S. Cao, L. Mo, D. Chu, G. Zhao, K. Zhao, Z. Yang, S. F. Liu, *ACS Appl. Mater. Interfaces* **2020**, *12*, 16592; c) S. S. Jia, Y. R. Xiao, M. X. Hu, X. L. He, N. Bu, N. Li, Y. C. Liu, Y. X. Zhang, J. Cui, X. D. Ren, K. Zhao, M. Liu, S. B. Wang, N. Y. Yuan, J. N. Ding, Z. Yang, S. Z. Liu, *Adv. Mater. Technol.* **2021**, *7*, 6; d) Y. Zhang, Y. Liu, Z. Xu, H. Ye, Z. Yang, J. You, M. Liu, Y. He, M. G. Kanatzidis, S. Liu, *Nat. Commun.* **2020**, *11*, 2304.

[8] a) X.-D. Wang, Y.-H. Huang, J.-F. Liao, Z.-F. Wei, W.-G. Li, Y.-F. Xu, H.-Y. Chen, D.-B. Kuang, *Nat. Commun.* **2021**, *12*, 1202; b) Y.-W. Jang, S. Lee, K. M. Yeom, K. Jeong, K. Choi, M. Choi, J. H. Noh, *Nat. Energy* **2021**, *6*, 63.

[9] a) R. Wang, J. Wang, S. Tan, Y. Duan, Z.-K. Wang, Y. Yang, *Trends Chem.* **2019**, *1*, 368; b) Z. Cai, X. Wu, H. Liu, J. Guo, D. Yang, D. Ma, Z. Zhao, B. Z. Tang, *Angew. Chem., Int. Ed. Engl.* **2021**, *60*, 23635; c) C. Tian, S. Zhao, T. Guo, W. Xu, Y. Li, G. Ran, *Opt. Mater.* **2020**, *107*, 110130; d) P. Gui, H. Zhou, F. Yao, Z. Song, B. Li, G. Fang, *Small* **2019**, *15*, 39.

[10] a) Q. Shang, M. Li, L. Zhao, D. Chen, S. Zhang, S. Chen, P. Gao, C. Shen, J. Xing, G. Xing, B. Shen, X. Liu, Q. Zhang, *Nano Lett.* **2020**, *20*, 6636; b) G. Liu, S. Jia, J. Wang, Y. Li, H. Yang, S. Wang, Q. Gong, *Nano Lett.* **2021**, *21*, 8650.

[11] a) J. M. Wu, L. X. Wang, A. B. Feng, S. Yang, N. Li, X. M. Jiang, N. A. Q. Liu, S. D. Xie, X. B. Guo, Y. J. Fang, Z. L. Chen, D. R. Yang, X. T. Tao, *Adv. Funct. Mater.* **2022**, *32*, 9; b) F. Yao, J. Peng, R. Li, W. Li, P. Gui, B. Li, C. Liu, C. Tao, Q. Lin, G. Fang, *Nat. Commun.* **2020**, *11*, 1194.

[12] a) X. Xu, W. Qian, J. Wang, J. Yang, J. Chen, S. Xiao, Y. Ge, S. Yang, *Adv. Sci.* **2021**, *8*, 2102730; b) P. Zhang, Y. Hua, Y. Xu, Q. Sun, X. Li, F. Cui, L. Liu, Y. Bi, G. Zhang, X. Tao, *Adv. Mater.* **2022**, *34*, 2106562; c) S. Deumel, A. Van Breemen, G. Gelinck, B. Peeters, J. Maas, R. Verbeek, S. Shanmugam, H. Akkerman, E. Meulenkamp, J. E. Huerdler, M. Acharya, M. García-Batlle, O. Almora, A. Guerrero, G. Garcia-Belmonte, W. Heiss, O. Schmidt, S. F. Tedde, *Nat. Electron.* **2021**, *4*, 681.

[13] S. Yakunin, M. Sytnyk, D. Kriegner, S. Shrestha, M. Richter, G. J. Matt, H. Azimi, C. J. Brabec, J. Stangl, M. V. Kovalenko, W. Heiss, *Nat. Photonics* **2015**, *9*, 444.

[14] a) Y. Wu, J. Feng, Z. Yang, Y. Liu, S. Liu, *Adv. Sci.* **2023**, *10*, 2205536; b) B. Shabbir, J. C. Yu, T. Warnakula, R. A. W. Ayyubi, J. A. Pollock, M. M. Hossain, J.-E. Kim, N. Macadam, L. W. T. Ng, T. Hasan, D. Vak, M. J. Kitchen, J. J. Jasieniak, *Adv. Mater.* **2023**, *35*, 2210068; c) K. Sakhatskyi, B. Turedi, G. J. Matt, E. Wu, A. Sakhatska, V. Bartosh, M. N. Lintangpradipto, R. Naphade, I. Shorubalko, O. F. Mohammed, S. Yakunin, O. M. Bakr, M. V. Kovalenko, *Nat. Photonics* **2023**, *17*, 510; d) P. Jin, Y. Tang, D. Li, Y. Wang, P. Ran, C. Zhou, Y. Yuan, W. Zhu, T. Liu, K. Liang, C. Kuang, X. Liu, B. Zhu, Y. Yang, *Nat. Commun.* **2023**, *14*, 626; e) J. Jiang, M. Xiong, K. Fan, C. Bao, D. Xin, Z. Pan, L. Fei, H. Huang, L. Zhou, K. Yao, X. Zheng, L. Shen, F. Gao, *Nat. Photonics* **2022**, *16*, 575.

[15] a) L. Zhao, Y. Zhou, Z. Shi, Z. Ni, M. Wang, Y. Liu, J. Huang, *Nat. Photonics* **2023**, *17*, 315; b) X. Liu, Q. Zhang, D. Zhao, R. Bai, Y. Ruan, B. Zhang, F. Li, M. Zhu, W. Jie, Y. Xu, *ACS Appl. Mater. Interfaces* **2022**, *14*, 51130.

[16] a) Y.-H. Deng, Z.-Q. Yang, R.-M. Ma, *Nano Converg* **2020**, *7*, 25; b) L. Han, C. Liu, L. Wu, J. Zhang, *J. Cryst. Growth* **2018**, *501*, 27; c) H.-S. Rao, W.-G. Li, B.-X. Chen, D.-B. Kuang, C.-Y. Su, *Adv. Mater.* **2017**, *29*, 1602639.

[17] M. I. Saidaminov, A. L. Abdelhady, B. Murali, E. Alarousu, V. M. Burlakov, W. Peng, I. Dursun, L. Wang, Y. He, G. Maculan, A. Goriely, T. Wu, O. F. Mohammed, O. M. Bakr, *Nat. Commun.* **2015**, *6*, 7586.
[18] M. I. Saidaminov, V. Adinolfi, R. Comin, A. L. Abdelhady, W. Peng, I. Dursun, M. Yuan, S. Hoogland, E. H. Sargent, O. M. Bakr, *Nat. Commun.* **2015**, *6*, 8724.
[19] Q. Dong, Y. Fang, Y. Shao, P. Mulligan, J. Qiu, L. Cao, J. Huang, *Science* **2015**, *347*, 967.
[20] a) W. Pan, H. Wu, J. Luo, Z. Deng, C. Ge, C. Chen, X. Jiang, W.-J. Yin, G. Niu, L. Zhu, L. Yin, Y. Zhou, Q. Xie, X. Ke, M. Sui, J. Tang, *Nat. Photonics* **2017**, *11*, 726; b) N. Bu, S. Jia, Y. Xiao, H. Li, N. Li, X. Liu, Z. Yang, K. Zhao, S. (F.). Liu, *J. Mater. Chem. C* **2022**, *10*, 6665.
[21] H. Wei, Y. Fang, P. Mulligan, W. Chuirazzi, H.-H. Fang, C. Wang, B. R. Ecker, Y. Gao, M. A. Loi, L. Cao, J. Huang, *Nat. Photonics* **2016**, *10*, 333.
[22] E. Samei, M. J. Flynn, D. A. Reimann, *Med. Phys.* **1998**, *25*, 102.